nature physics

SUPPLEMENTARY INFORMATION

DOI: 10.1038/NPHYS2456

Direct observation of competition between superconductivity and charge density wave order in $YBa_2Cu_3O_{6.67}$

J. Chang, E. Blackburn, A. T. Holmes, N. B. Christensen, J. Larsen, J. Mesot, Ruixing Liang, D. A. Bonn, W. N. Hardy, A. Watenphul, M. v. Zimmermann, E. M. Forgan, S. M. Hayden

Note: to make this document complete, some text in the Methods section is repeated here.

S1: EXPERIMENTAL DETAILS

Our experiments used 100 keV hard x-ray synchrotron radiation from the DORIS-III storage ring at HASYLAB, Hamburg, Germany. We installed a recently developed 17 T horizontal cryomagnet designed for beamline use [34] on the triple axis diffractometer at beamline BW5 [35]. This was operated using Ge-gradient Si(111) crystals as monochromator and analyser [36, 37], with the rocking width tuned to 35 arc sec. The sample was mounted by gluing it over a hole in a temperature-controlled aluminium plate within the cryomagnet vacuum, and was thermally shielded by thin Al and aluminised mylar foils glued to this plate. The sample temperature could be controlled over the range ~ 2-300 K. The incoming and outgoing beams passed through 1 mm thick aluminium cryostat vacuum windows, which gave a maximum of ~±10° input and output angles relative to the field direction, which was parallel to the sample ***c***-axis within < 1°. Between the beam access windows and the sample plate, there were further aluminium foil thermal radiation shields at liquid nitrogen temperature. A 2 mm square aperture collimated the incoming beam, so that it passed mainly through the part of the sample over the hole in the aluminium plate, greatly reducing background scattering by the plate. Further slits before the analyser and the detector removed scattering by the cryostat windows and nitrogen shields. The scattering plane (***a****-***c****) was horizontal. The cryomagnet was mounted on a rotation stage with a goniometer giving χ tilt about the field axis. The sample was initially mounted with its ***a***-axis nearly horizontal. The χ goniometer allowed the exact alignment of this axis using the (2 0 0) Bragg peak and could also be used for low-resolution scans in the ***b**** direction. Magnetic fields were applied with the sample heated above T_c; it was then field-cooled to base temperature. When fields were applied, minor changes in the position and angle of the sample holder were observed; these were corrected by use of horizontal and vertical motion stages under the cryostat rotation stage, and by realigning on the (2 0 0) Bragg peak. During temperature scans, realignment on the (2 0 0) Bragg peak was performed automatically at every temperature point to ensure that all measurements were centred. After results had been obtained with the ***a***-axis horizontal, the sample was remounted with the ***b***-axis horizontal for additional measurements.

We briefly compare hard X-ray diffraction with the resonant soft X-ray technique used in Refs. 14, 15 and 32. Due to our high energy and large incoming wavevector, we can measure in transmission and access a large region of reciprocal space, whereas soft X-rays have to be used in reflection and can access a rather limited region of reciprocal space. The resonant technique can be tuned to greatly enhance the signal from specific copper (or oxygen) sites, whereas hard X-rays detect all the atoms in the crystal. The "contrast" seen by the soft X-ray technique appears to arise from the spatial variation of the energy of the Cu *L*-resonance [32], and presumably with calibration could measure the magnitude of this, whereas the hard X-ray technique is sensitive to atomic motions, and with calibration can give information about their magnitude. In addition, we have been able to make use of very high magnetic fields to demonstrate how the suppression of superconductivity enhances the CDW order.

S2: SAMPLE INFORMATION

The $YBa_2Cu_3O_{6.67}$ sample had dimensions $a \times b \times c = 3.1 \times 1.7 \times 0.6$ mm^3 and mass 18 mg. The superconducting transition temperature $T_c = 67$ K (width: 10%-90% = 1.1 K) was derived from a Zero-Field-Cooled magnetization curve at 0.1 mT. The single crystal was 99% de-twinned (Fig. S1) and the Cu-O chains were ordered with the ortho-VIII structure by standard procedures [12]. Due to the ortho-VIII ordering of the Cu-O chains, structural peaks are expected at h values that are multiples of $^1/_8$. The strongest of these are expected [38] at (n +$^3/_8$, 0, 0) and (n +$^5/_8$, 0, 0) and are seen in the top panel of Fig. S2. They have a Lorentzian profile.

The four oxygen-ordering peaks around the (200) Bragg peak have an average Lorentzian h-linewidth (HWHM) of $\lambda_h \sim 3.9 \times 10^{-2}$ rlu $\equiv 6.4 \times 10^{-2}$ Å^{-1}. This corresponds to an (exponential) correlation length of about 16 Å - much shorter than the (Gaussian) correlation length of the CDW peaks reported in this work. The CDW peaks are found along ℓ on the Lorentzian tails of the oxygen-ordering peaks. The ℓ-dependence of one of these peaks is shown in the bottom panel of Fig. S2. It is broad, indicating (as observed before [8]) that the CuO chain ordering is not very coherent in the **c**-direction. The weakest oxygen-ordering peak is found at ($^{13}/_8$, 0, 0). For this reason, the bulk of this work on the CDW modulation focused on the (1.696, 0, 0.5) reflection.

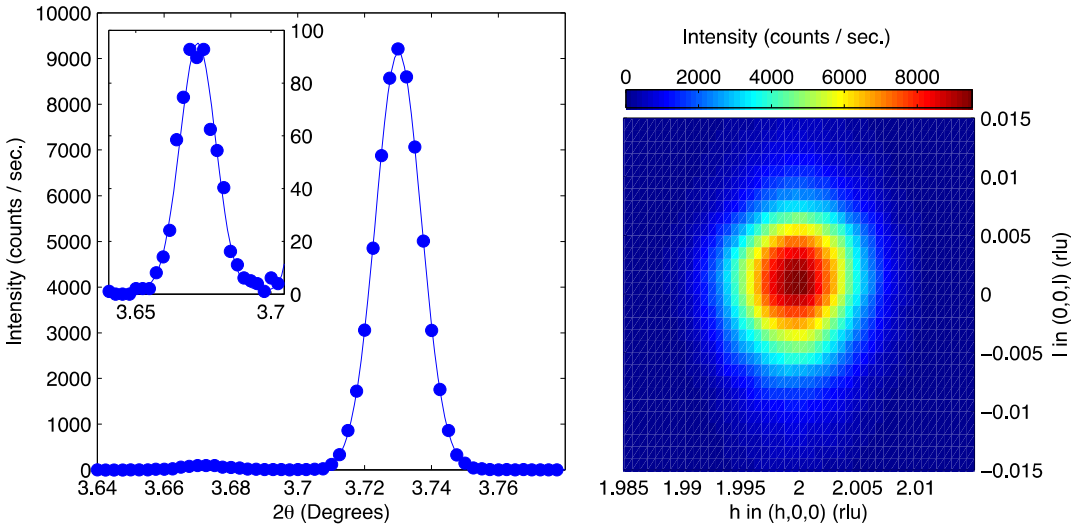

Figure S1: Bragg peaks and instrumental resolution

Left panel: Intensity versus scattering angle 2θ, for the (2 0 0) Bragg reflection, taken at base temperature ($T = 2$ K) and zero applied magnetic field. From these data, the lattice constant $a = 3.81$ Å was found. The structure factors of the (2 0 0) and (0 2 0) reflections are nearly identical, so the zoom on the weaker reflection, in the inset, shows that our crystal is 99% detwinned and that $b = 3.87$ Å. The blue lines are resolution limited Gaussian fits.
Right panel: Map of intensity versus h and ℓ around the (2 0 0) Bragg peak. The elliptical shape reveals the instrumental resolution in the (h, ℓ) plane. Its Gaussian standard deviation σ at the (2 0 0) Bragg peak is $(3.82, 16.4, 5.2) \times 10^{-3}$ reciprocal lattice units (r.l.u.). For the data shown in both left and right panels the scattered beam was attenuated by factor of $\sim 3.5 \times 10^5$, to prevent detector overload.

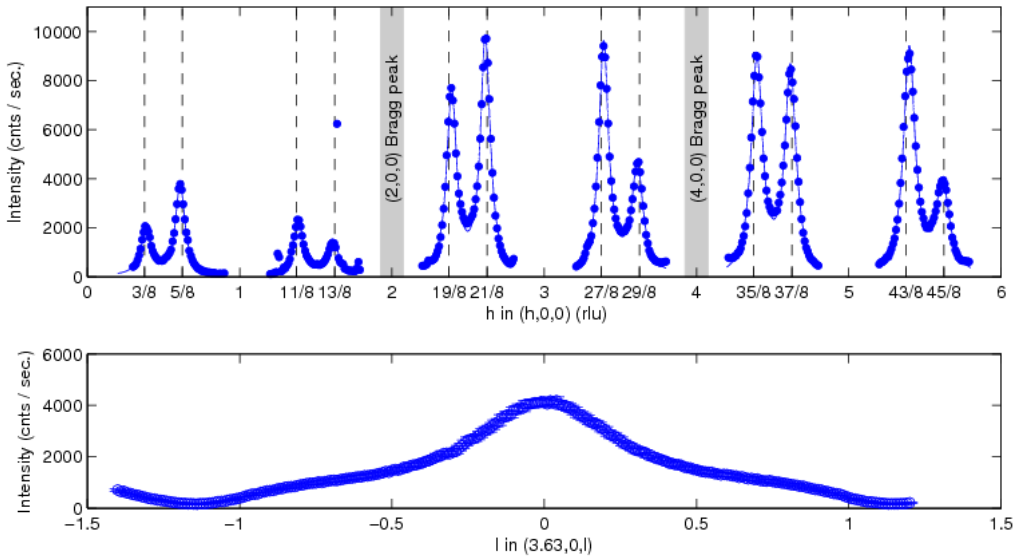

Figure S2: Ortho-VIII oxygen ordering peaks.
Top panel: Scan along (h, 0, 0) measured at T = 2 K and zero applied magnetic field. Ortho-VIII structural peaks, as indicated by vertical dashed lines, were observed at (n $+^{3}/_{8}$, 0, 0) and (n $+^{5}/_{8}$, 0, 0) from n = 0 to 5. The weakest oxygen-ordering peak is found at (13/8, 0, 0). The strong Bragg peak positions (2, 0, 0) and (4, 0, 0) are indicated by the vertical gray shaded bands. Solid blue lines are Lorentzian fits to the data.
Bottom panel: Scan along (3.63, 0, ℓ) under the same conditions. The oxygen order is three-dimensional but weakly correlated along the z-direction.

S3: ANALYSIS OF THE CHARGE DENSITY WAVE PEAKS.

Background subtraction.
The diffracted intensities from the CDW, shown in Fig. 1, are composed of an incommensurate lattice modulation peak on a smoothly-varying background. The background along (h, 0, 0.5) mainly originates from the tails of the ortho-VIII peaks shown in Fig. S2. It varies strongly from one Brillouin zone to another; for example, the background around (2.7, 0, 0.5) is an order of magnitude larger than around (1.7, 0, 0.5). In Fig. S3, we show some CDW diffracted intensities before and after the background $B(Q)$ (see below) has been subtracted. The background has essentially no field dependence (Fig. 1a-c) so subtracting the zero-field from high-field data is a simple way to eliminate the background. This reveals the field-enhanced signal inside the superconducting state (see Fig. 1a-d).

As there is a weak temperature dependence in the background (see Fig. 1a-c of the main text), it is not possible to eliminate it by subtracting a high-temperature curve. Therefore, to obtain the temperature dependences shown in Fig. 2, we fitted the data to a Gaussian function $G(Q)$ and modelled the background by a second order polynomial $B(Q) = c_0+c_1Q+c_2Q^2$. The constants c_0, c_1 and c_2 have a small but significant temperature dependence. The low counting statistics resulted in Gaussians fitting equally well as other possible lineshapes such as Lorentzians.

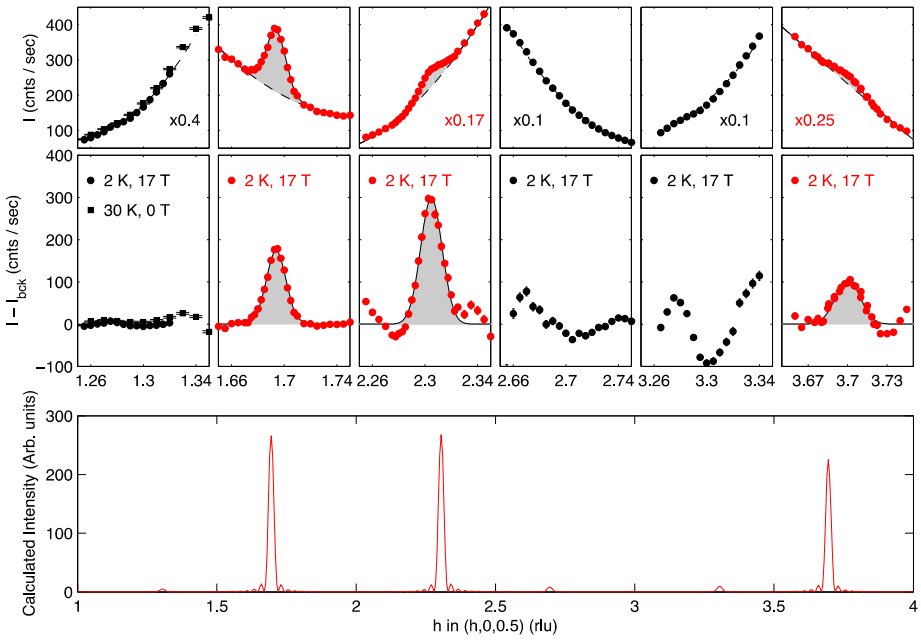

Figure S3: CDW reflections along the (*h*, 0, 0.5) direction.
Top panels: Diffracted intensity as a function of momentum (*h*, 0, 0.5) through some expected CDW satellite positions $\boldsymbol{Q}_{CDW} = (n \pm \delta_1, 0, 0.5)$ where $\delta_1 \sim 0.305$ rlu. Dashed lines indicate the background modelled by $B(Q) = c_0+c_1Q+c_2Q^2$. To make the backgrounds comparable, the intensities have been scaled down by the factors shown. The best signal to background ratio is found for the $\boldsymbol{Q}_{CDW} = (2 - \delta_1, 0, 0.5)$ peak. **Middle panels:** The same data but with the background subtracted. The intensity due to the CDW is strongest at the $(2 + \delta_1, 0, 0.5)$ reflection and not observed for $(1 + \delta_1, 0, 0.5)$ and $(3 \pm \delta_1, 0, 0.5)$ (black points). **Bottom panel:** A model calculation (see section S4) of the scattered intensity for the bilayer-centred structure (Fig. 3a) predicts that the most intense satellites should be observed around the strong Bragg peaks (2 0 0) and (4 0 0). Similar results were obtained for the chain-centred structure (Fig. 3b).

Correlation lengths

The signal-to-background ratio is best for the $(2\text{-}\delta_1, 0, 0.5)$ peak due to the weaker structural ortho-VIII peak (see Fig. S2). From the Gaussian fits to the $(2\text{-}\delta_1, 0, 0.5)$ satellite peak at 2 K and 17 T we can estimate the correlation length ξ along the three crystal axis directions. We define $\xi = 1 / \sigma$ where $\sigma = (\sigma_{fit}^2 - \sigma_R^2)^{0.5}$ is the fitted Gaussian standard deviation corrected for the instrument resolution σ_R (Fig. S1) and expressed in $Å^{-1}$. Along the ***a***-axis direction, we find $\sigma = 6.4 \times 10^{-3}$ r.l.u. $\equiv 1.1 \times 10^{-2}$ $Å^{-1}$ and hence $\xi_a = 95 \pm 5$ Å. Deconvolving the poor instrumental resolution along the ***b***-axis direction yields a similar correlation length $\xi_b \sim \xi_a$. The correlation length ξ_c along the ***c***–axis is discussed in the next section.

S4: MODELLING OF THE CDW ORDER.

X-rays are primarily scattered by the electronic charges in a crystal, but there is also weak non-resonant scattering by magnetic order [39]. Assuming a magnetic moment around 1 μ_B per unit cell, we calculate that any magnetic signal would be at least 3 orders of magnitude weaker than our observed satellites; hence our signal must originate from charge and not magnetic scattering. Our measurements *alone* do not rule out magnetic ordering *accompanying* the lattice modulation (such magnetic ordering - as estimated above - would not be detectable), but the field-independence of the modulation seen in the normal state strongly suggests no magnetic effects (apart from those on the superconductivity) and NMR measurements [13] on an ortho-VIII sample and soft X-ray measurements [32] on an ortho-III sample also rule out magnetic ordering. A charge density wave causes a redistribution of the electronic charge in space. There are two connected effects. (1) The charge (valence) associated with each atom can vary in space. (2) Electron-phonon coupling means that there is a modulation of the atomic positions associated with a CDW [15, 40]. Thus, *displacement* of the atoms (and their charge clouds) gives rise to a second contribution to the charge redistribution. As discussed in [15] and section S7 the atomic displacement term gives the dominant contribution.

A modulation of the atomic positions can be expressed in the form

$$\boldsymbol{r}_i = \boldsymbol{r}_i^0 + \sum_k \boldsymbol{u}_k \sin(\boldsymbol{q}_k \cdot \boldsymbol{r}_i^0), \tag{S1}$$

where $\boldsymbol{r}_i^0$ are the unperturbed atomic positions and $\boldsymbol{u}_k$ is the amplitude of the Fourier component with wavevector $\boldsymbol{q}_k$. Such a modulation gives rise to new satellite peaks at positions $\boldsymbol{Q} = \boldsymbol{\tau} + n\boldsymbol{q}_k$, where $\boldsymbol{\tau}$ denotes the reciprocal lattice points,. The intensity of the satellite peaks is proportional to the square of the component of the displacement parallel to $\boldsymbol{Q}$. (The displacement of ions *within* Bragg planes has no effect on the X-ray scattering, only displacement perpendicular to the planes.) Because $\boldsymbol{c}^*$ is about 3 times smaller than $\boldsymbol{a}^*$, we note that $\boldsymbol{Q}$ is nearly parallel to $\boldsymbol{a}^*$, so the X-rays will be much more sensitive to ionic displacements *along* $\boldsymbol{a}$, than those which may occur along $\boldsymbol{c}$.

To model our results, we computed the expected scattering distributions for various patterns of lattice modulation (see Fig. 3). We consider finite arrays of atoms with sizes up to 500 unit cells in each direction. The structure factor is then given by,

$$F(\boldsymbol{Q}) = \frac{1}{N_{\text{cell}}} \sum_j f_j(Q) \exp(i\boldsymbol{Q} \cdot \boldsymbol{r}_j), \tag{S2}$$

where the scattered intensity is given by $I = |F(\boldsymbol{Q})|^2$, $f_j(Q)$ are the atomic scattering amplitudes (Using ionic scattering amplitudes makes no qualitative difference to our results.), $\boldsymbol{r}_j$ are the ionic positions and the sum is over the whole array. We take $\boldsymbol{u}_k$ parallel to $\boldsymbol{a}$, since we are only sensitive to displacements parallel to the scattering vector $\boldsymbol{Q}$, which is close to this direction. Two models which are consistent with the data (see section S9 for further discussion) are the “bilayer

centred" and "chain centred" modulations (see Fig. 3(a, b) of the main text). For the bilayer centred model we have $\boldsymbol{q}_+=(\delta_1, 0, 0.5)$, $\boldsymbol{q}_-=(\delta_1, 0, -0.5)$ and $u_+ = -u_- = u/2$, giving:

$$\sum_k \boldsymbol{u}_k \sin(\boldsymbol{q}_k \cdot \boldsymbol{r}_i^0) = u\hat{\boldsymbol{x}} \sin(\pi z / c)\cos(2\pi\delta_1 x / a). \tag{S3}$$

(We take $z = 0$ in a chain layer.) Similarly for the chain centred model we have, $\boldsymbol{q}_+=(\delta_1, 0, 0.5)$, $\boldsymbol{q}_-=(\delta_1, 0, -0.5)$ and $u_+ = u_- = u/2$,

$$\sum_k \boldsymbol{u}_k \sin(\boldsymbol{q}_k \cdot \boldsymbol{r}_i^0) = u\hat{\boldsymbol{x}} \cos(\pi z / c)\cos(2\pi\delta_1 x / a). \tag{S4}$$

Both the "bilayer-centred" and "chain centred" models give peaks (among others) at $(h, 0, 0.5)$ where $h = 1.696$, 2.304 and 3.696 and predict very weak peaks at $h = 1.304$, 2.696 and 3.304 where the satellites were not detected in our experiment (see Fig. S3). The "bilayer centred" and "chain centred" models have 2-$\boldsymbol{q}$ counterparts (These consist of a superposition of modulations along both $\boldsymbol{a}$ and $\boldsymbol{b}$.), which are also consistent with the data. We argue in the main text that the structure is likely to be 2-$\boldsymbol{q}$., and for the bilayer-centred model (see Fig. 3(c)) it has the form:

$$\sum_k \boldsymbol{u}_k \sin(\boldsymbol{q}_k \cdot \boldsymbol{r}_i^0) = u\hat{\boldsymbol{x}} \sin(\pi z / c)\cos(2\pi\delta_1 x / a) + u\hat{\boldsymbol{y}} \sin(\pi z / c)\cos(2\pi\delta_2 y / b). \tag{S5}$$

The results of modelling the ℓ-dependence of the intensity are shown in Fig. S4 and compared with the data from Fig. 1d. We find good agreement with our data in Fig. S4 if the coherence of ordering of adjacent CuO_2 bilayers has a scattering amplitude which falls off along z with a Gaussian width of 0.6 unit cells.

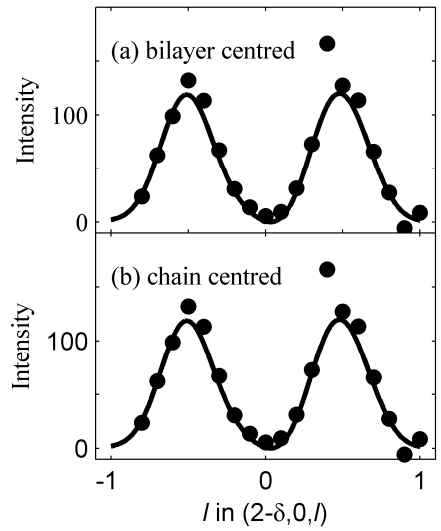

Figure S4: Calculations of ℓ-dependence of satellite intensity for two models.

The bilayer-centred (a) and chain-centred models (b) are fully described in the text.. Filled circles are data points from Fig. 1d. We see that both models are equally consistent with the data presented here.

S5: ESTIMATE OF THE MODULATION AMPLITUDE.

The incommensurate satellite peaks appear around the strong Bragg peaks (2, 0, 0) and (4, 0, 0). In fact, it is possible to derive a simple relation between the Bragg and satellite peak intensities as we will now show. Let us consider the CDW peak at $\boldsymbol{Q} = (2-\delta_1, 0, 0.5)$; this can be regarded as being a satellite of both (2, 0, 0) and (2, 0, 1) of the parent crystal, with $\boldsymbol{q}$-vectors $(-\delta_1, 0, \pm 0.5)$. However the (2, 0, 1) reflection is very weak, so that it is a good approximation to regard the peak as a satellite of the (2, 0, 0) alone. In this case, neglecting the small variation of form factor with Q, the integrated intensity of the satellite compared with that of the (2, 0, 0) may be calculated directly. Taking the maximum amplitude of lattice distortion to be $\boldsymbol{u}$, varying sinusoidally with x and z, one obtains:

$$\frac{I_{\boldsymbol{Q}}}{I_{200}} \sim \left(\frac{\boldsymbol{Q}.\boldsymbol{u}}{4}\right)^2 \sim \left(\frac{1.7\times 2\pi u}{4a}\right)^2 \sim 7.1\left(\frac{u}{a}\right)^2 \qquad \text{(S6)}$$

The intensity ratio between the satellite and Bragg reflection is therefore given by the amplitude of the lattice distortion. This result compares well with the modelling (discussed in section S4), which gives the exact numerical factor 7.7 for the bilayer-centred pattern of displacements.

It is thus possible to estimate the value of u directly from our experiment. The integrated intensity of a peak is proportional to the product of the peak count rate with the Gaussian widths in h, k and ℓ. For the (2, 0, 0) Bragg reflection at 2 K and 17 T, we have I_{200} = 9500 counts /sec × 0.00382(8) × 0.0164(5) × 0.0052(2) × attenuator factor (see caption of Fig. S1). For the same conditions, $I_{\boldsymbol{Q}}$ = 170 counts / sec × .0073(2) × 0.0191(2) × 0.16(1) (Fig. 2), leading us to estimate $I_{200} / I_{\boldsymbol{Q}} \sim 3 \times 10^5$. Following Eq. S6, we therefore estimate that $u / a \sim (7.7 \times 3 \times 10^5)^{-0.5} \sim 7 \times 10^{-4}$. Our estimate has a considerable error bar due to the large amount of attenuation used in measuring the (2, 0, 0) peak. The intensity of this peak may also be reduced by extinction effects. Our estimate of u / a under these conditions should therefore be regarded as an upper limit.

S6: ESTIMATES OF QUANTITIES INVOLVED IN THE LATTICE MODULATION

Effects on X-ray scattering of displacements *versus* charge ordering

X-ray scattering is sensitive to the charge distribution of the electrons in a solid. Scattering can be enhanced by tuning the X-ray photon energy to an atomic core transition, i.e. resonant X-ray scattering [14, 15, 32]. However, here we use non-resonant scattering, which is sensitive to the overall charge distribution. A charge density wave causes a redistribution of the electronic charge in space. There are two connected effects:

(1) The charge (valence) associated with each atom can vary in space. We denote this contribution as $\rho^v(x)$.

(2) Electron-phonon coupling means that there is a modulation of the atomic positions $x_i = x_i^0 + u\sin(q\,x_i^0)$ associated with the CDW. Thus, displacement of the atoms (and their charge clouds) gives rise to a second contribution to the charge redistribution $\rho^u(x)$.

It is this second contribution to which we are most sensitive. We demonstrate this in the following approximate 1-D calculation.

If the CDW is driven by the CuO_2 bilayers, then assuming that each copper contributes one electron, and that the electronic states are rearranged on an energy scale $\Sigma = \Sigma_{\mathrm{CDW}} \approx 1.76 k_B T_{CDW}$ ≈20 meV [40], an upper estimate of the CDW "valence" modulation is,

$$\rho^{v}(x) = \frac{2e}{a}\left[1 + \Sigma_{CDW}\, N(\varepsilon_F)\cos(qx)\right], \tag{S8}$$

where $2e/a$ is the uniform electron density (a is the lattice spacing) of the bilayer conduction electrons in the absence of the CDW, and $N(\varepsilon_F) \approx 2.8$ States eV^{-1} $(\mathrm{CuO_2})^{-1}$ (≡ 5.6 per bilayer per unit cell) [41].

To estimate the effect of the lattice modulation, we start from a uniform electron density of all electrons $\rho_0 = Ze/a$ and make the coordinate transformation $x = x^0 + u\sin(qx^0)$, assuming that $\rho_0\, dx^0 = \rho(x)\, dx$, we have:

$$\rho^{u}(x) = \frac{Ze}{a}\left[1 + uq\cos(qx)\right] \tag{S9}$$

We estimate the displacement due to the CDW from the mean field theory of a Peierls transition [40] $M\omega_q^2 u^2 = \Sigma_{CDW}^2 N(\varepsilon_F)$. Here M is the unit cell mass, ω_q is the frequency of the acoustic phonon (estimated at $\hbar\omega_q \approx 5$ meV) which becomes frozen at the CDW transition. Thus $u = \left(\Sigma_{CDW}^2 N(\varepsilon_F)/M\omega_q^2\right)^{1/2} \approx 0.003$ Å. With lattice parameter, a = 3.81 Å, this gives u / a $\sim 8 \times 10^{-4}$, which is very close to that estimated from our experiments.

The ratio of the contributions to the intensity of the Bragg peak at wavevector $\boldsymbol{q}$ is

$$\frac{I^u}{I^v} = \left(\frac{Zuq}{2\Sigma_{CDW} N(\varepsilon_F)}\right)^2 \approx 600. \tag{S10}$$

This clearly demonstrates that we are mainly sensitive to the atomic displacements.

Energy changes in a CDW

Charge density waves may form by a variety of mechanisms. The best understood is the Peierls mechanism. However a CDW may also be driven by electron interactions [42]: in particular, in the *t-J* model there is a tendency of holes to separate when in the presence of AFM order [43, 44]. This may persist into the region of doping here, where antiferromagnetism is only seen as fluctuations, not as order. It may then be that nesting of the Fermi surface is controlling the ***q***-vector at which we see a CDW, or it may be that details of the interactions integrated over the whole band structure control the ordering wavevector [45]. We do not attempt these calculations; instead, we make *order of magnitude estimates* of various energies involved in forming a CDW. Whatever the mechanism, we expect, and find, that these energies are comparable with, but smaller than, the condensation energy of the superconducting state. For optimally-doped YBCO, the thermodynamic critical field is $\mu_0 H_c(T = 0) \sim 1.1$ T [41], giving a condensation energy density $\sim 4.8 \times 10^5$ Jm^{-3}, so the CDW energy densities calculated below for our sample with lower T_c

should be smaller than this value. (Note that the value of the transition temperature T_{CDW} will not just be determined by energy, but also by the entropy contributions to the *free* energy, which at high temperatures will favour the higher-entropy un-gapped state, which gives $k_B T_{CDW} \sim \Sigma$.)

Energy change of conduction electrons

The CDW is expected to give rise to a gap or modification of the electron dispersion curve over a range of energies Σ. Since the CDW competes with the superconductivity, which has T_c = 67 K, this confirms that Σ is of order 10-20 meV. The competition arises because gapped electrons cannot contribute to superconductivity, and conversely the reduced DOS at the Fermi level due to superconductivity reduces the energy reduction available to the CDW. Since superconductivity reduces the CDW amplitude (Fig. 2a), they must have similar energy scales.

The gapping or reduction of DOS by the CDW, if it occurs on, say, ¼ of the Fermi surface, will lower the energy of the electrons by:

$$\delta E \sim \frac{1}{2}\frac{N(E_F)}{4}\Sigma^2 \qquad \text{(S11)}$$

The DOS (both spins) for YBCO $N(E_F) \sim 2.8$ $(\text{eV})^{-1}$ $(\text{CuO}_2)^{-1}$ [41], and using the value Σ = 15 meV in Eqn. (S11), with a unit cell volume of 1.7×10^{-28} m^3, we estimate the reduction of the conduction electron energy by the CDW to be $\sim 1.5 \times 10^5$ Jm^{-3}.

Energy cost of lattice distortion

This reduction will partly be counteracted by the positive elastic energy density of the lattice distortion.

$$\delta E_{elastic} = \tfrac{1}{2} C \left\langle \varepsilon^2 \right\rangle , \qquad \text{(S12)}$$

where ε is the strain and C is the appropriate elastic constant (for an indication of the order of magnitude, we will take the bulk modulus = 1.3×10^{11} Pa) [46]. The amplitude of the strain ε_0 is related to the maximum amplitude of ionic motion in the CDW by:

$$\varepsilon_0 = \delta_1 u \sim 0.3\frac{2\pi}{a}u , \qquad \text{(S13)}$$

with $\left\langle \varepsilon^2 \right\rangle = \tfrac{1}{2}\varepsilon_0^2$, and taking $u / a \sim 7 \times 10^{-4}$, we obtain $\delta E_{elastic} \sim 6 \times 10^4$ Jm^{-3}. This increase in energy is noticeably less than the estimated energy reduction of the electrons.

Estimate of matrix element for interaction of distortion with conduction electrons

The ionic displacements due to the CDW are expected to give rise to a modification of the conduction electron energy dispersion over an energy range of order Σ. We can use the expression (S13) for the amplitude of the lattice strain ε_0, which is close to its maximum at the CuO_2 planes for the bilayer-centred model. We assume that the major effect of this strain is to modify the nearest-neighbour hopping matrix element t by an amount δt, which will give a gap in the electronic dispersion curve $\sim \delta t$. To estimate this, we need the strain-dependence of t. This might be obtained from first-principles, but we use experiment instead [47]. We assume that the

dominant effect in the pressure-dependence of the normal-state resistivity ρ of YBCO is the change in bandwidth ($\propto t$) due to the strain. The experimental value (independent of $T > T_c$) [48] is:

$$\frac{1}{\rho}\frac{d\rho}{dp} = \text{-1\% / kbar} = \text{-}10^{-10} \text{ / Pa}$$

Using the bulk modulus = 1.3×10^{11} Pa this gives:

$$\frac{V}{\rho}\frac{d\rho}{dV} = 13 \text{ and with } \frac{dx}{x} \sim \frac{1}{3}\frac{dV}{V}, \text{ we have } \frac{x}{\rho}\frac{d\rho}{dx} = 39$$

By assumption, $\frac{x}{\rho}\frac{d\rho}{dx} = \frac{x}{t}\frac{dt}{dx} = 39$ also, so we expect $\frac{\delta t}{t} = 39\frac{\delta x}{x} = 39\varepsilon_0$

Using t = 0.38 eV [49], and the experimental value of $u/a \sim 7 \times 10^{-4}$, we calculate $\Sigma \sim \delta t \sim 20$ meV, which is close to the value expected.

In conclusion, the energies calculated in this section cannot be regarded as definitive, since they are order-of-magnitude estimates, but they indicate that the existence of CDW order is consistent with the known energetics of the YBCO system.

S7: LANDAU THEORY OF THE COMPETITION BETWEEN SUPERCONDUCTIVITY AND CDW

In this section, we demonstrate a simple Landau theory that captures the basic physics of competition between superconductivity and CDW order. It is related to more complicated Landau theories which have been applied in rather different circumstances [31,50-53]. We write down the homogeneous terms in the free energy, ignoring complications such as spatial variation of the superconducting order parameter, applied magnetic fields and higher-order terms in the Landau expansion. Superconductivity is represented by a (spatially averaged) order parameter Δ and the lattice displacements by an amplitude u, which acts as the order parameter of the CDW. With suitable normalisation, F may be written with a minimum of parameters:

$$F = (T - T_{CDW})u^2 + u^4 + (T - T_c)\Delta^2 + \alpha\Delta^4 + \beta u^2\Delta^2 . \qquad \text{(S14)}$$

Here, T_{CDW} is the temperature of onset of the CDW lattice modulation and is higher than T_c, which would be the superconducting critical temperature in the absence of any CDW; positive β represents competition between the two order parameters and causes a suppression of T_c:

$$T_c^{obs} = (T_c - \beta T_{CDW}/2)/(1 - \beta/2) \qquad \text{(S15)}$$

Below T_c^{obs}, Δ becomes nonzero and the temperature-dependence of the lattice modulation changes:

$$u^2 = (T_{CDW} - T)/2 \quad ; \; T \geq T_c^{obs}$$
$$u^2 = \frac{2\alpha(T_{CDW} - T) - \beta(T_c - T)}{(4\alpha - \beta^2)} \quad ; \; T \leq T_c^{obs} \qquad \text{(S16)}$$

Small α makes the superconductivity strong enough to *reduce* the amplitude of the lattice modulation at low temperatures (but $4\alpha > \beta^2$). A typical result for a particular set of parameters is shown in Fig. S5. Note that independent of the details of this model, it is an inevitable qualitative consequence of the competition between superconductivity and lattice modulation that the superconducting T_c is suppressed below the value it would otherwise achieve. We suggest that the shape of the "60 K plateau" in YBCO in this doping region is strongly affected by CDW order.

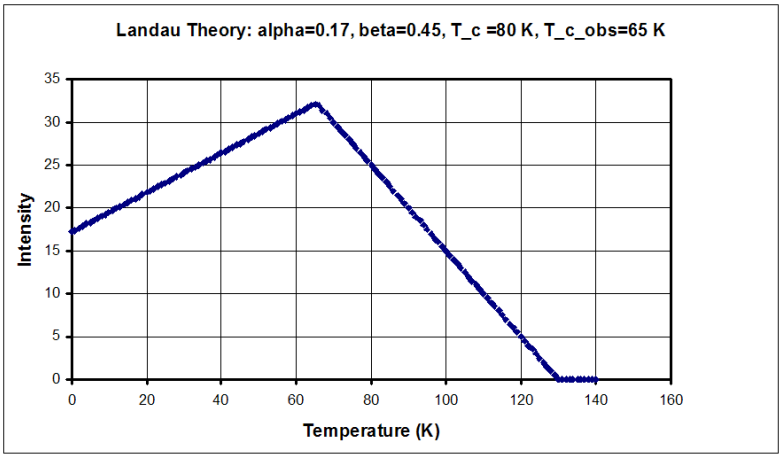

Figure S5: Typical numerical result of Landau theory
The intensity from the CDW is proportional to u^2, and sets in below T_{CDW}, which is set to 130 K. The superconducting T_c is suppressed below the value of 80 K, which it would have in the absence of the CDW, to 65 K. All temperature-dependences are linear because we have included only lowest-order terms in the Landau expansion.

We note that there exist microscopic theories of the competition between a CDW and BCS superconductivity [54, 55] and between a CDW and *d*-wave superconductivity [56, 57]. There is a qualitative similarity between the results of Refs. 56 and 57 and the Landau theory. We also note that the rise of the CDW intensity below T_{CDW} is slower, and its cusp near T_c is rather sharper than the fluctuation-free Landau theory. This may be due to the rather two-dimensional nature of the CDW order, which has a short ***c***-axis coherence length. It is possible instead that it arises because the CDW order is fluctuating at high temperatures. This is discussed further in the following section.

S8: THE NATURE OF THE CDW PHASE TRANSITION AND THE POSSIBILITY OF FLUCTUATING CDW ORDER

If the appearance of the CDW were a standard 2nd–order phase transition, we would expect to observe a jump in the heat capacity at T_{CDW} which would be comparable in size to that at T_c for superconductivity, since the two orders involve similar energy scales. In underdoped YBCO samples [58] no sharp peak in heat capacity has been observed at T_{CDW}, but there is a broad peak around this temperature in a sample of similar doping to ours. It should be noted that some of this excess heat capacity will arise from the formation of the pseudogap, but the data allow for a contribution from a broadened CDW ordering transition. However, since the CDW gap Σ is much smaller than ε_F, the critical region for fluctuations is expected to be narrow [59], so if the CDW

order is fluctuating, we cannot ascribe this to 3-dimensional critical fluctuations, because of the wide temperature range over which changes in coherence length are observed. It is possible that the quasi-two-dimensionality of the CDW order is also important. The finite (but reasonably long range) coherence that we observe is similar to the magnetic order seen in LSCO near to $^1/_8$ doping [60], where the c-axis coherence is also short. As a complicating factor, we note that pinning of a CDW by quenched disorder is always relevant in dimensions $d < 4$ [59]. Such pinning would be expected to smooth out the CDW transition [59] and again cause a finite correlation length in the CDW state, giving a "Bragg glass" well-known in the physics of flux line pinning [61]. However, if pinning of the CDW by the undoubted chain disorder were strong, then the correlation lengths we observe would tend to *decrease* as the temperature is lowered, and saturate, in contradiction with what we observe.

An incommensurate CDW (unlike a commensurate one) is not pinned to a perfect host lattice and therefore has phonon-like modes which have zero frequency at zero wavevector. However, we can also expect that if fluctuating, the dominant CDW fluctuations occur on an energy scale smaller than the superconducting gap, otherwise they would not compete with superconductivity. This energy scale is much smaller than the energy resolution of our hard X-ray experiment, so additional arguments, such as this and the following must serve to distinguish static or quasi-static order from dynamic fluctuations.

The long correlation length of the CDW order suggests that the fluctuations (if present) are on an energy scale even smaller than that of superconductivity. Since the CDW involves the lattice, any excitations cannot have a dispersion curve slope steeper than the speed of sound, v_s. Hence, if the width in q of the CDW order σ is due to fluctuations (it may not be), then the energy range of fluctuations should not exceed $\hbar v_s \sigma$. Inserting values of 4.6×10^3 ms^{-1} for v_s and 1.1×10^{-2} Å^{-1} for σ, we obtain an energy width of ~ 0.3 meV.

An even more restrictive limit on the timescale of any fluctuations is provided by NMR measurements [13], which indicate that, at least at 33.5 T and 67 K, the timescale is longer than the period of the nuclear Larmor frequency ~3 ns, corresponding to an energy width ~ μeV. It is possible that competing/intertwined orders result in the CDW being a (nearly) quantum phase transition, with quasi-static order over an extended temperature range. However, we strongly suspect that at low temperatures and high magnetic fields the CDW order is frozen.

Finally, we note that the relevant timescale for the CDW order to affect quantum oscillations at (say) 50 T is given by the cyclotron frequency, which gives a far less restrictive energy width of ~ 4 meV, so we would expect the CDW to affect the quantum oscillations. However, the quantum oscillation amplitude is greatly reduced if the CDW is not coherent over the area of a cyclotron orbit. At 50 T, the observed orbit has a radius ~ 170 Å.

S9: ELECTRONIC AND LATTICE STRUCTURE.

Fermi surface structure

The electronic structure of underdoped cuprates is still controversial. Transport and quantum oscillation experiments indicate that the Fermi surface at low temperature is reconstructed [9-11]. There is no consensus on how this happens or what the reconstructed Fermi surface looks like. Furthermore, it is hard to reconcile quantum oscillation experiments with angle resolved photoemission (ARPES) experiments, which suggest that the Fermi surface consists of "Fermi arcs". On the other hand, for overdoped cuprate superconductors, an excellent agreement between quantum oscillation, ARPES experiments and band structure calculations has been found [62-64]. These agree that the Fermi surface of a single-layered overdoped cuprate consists of a single large sheet, with the Fermi surface volume set by the doping level of the CuO_2 plane.

For YBCO, both ARPES [65] and LDA [28] calculations agree that the Fermi surface consist of bonding and anti-bonding sheets (due to bilayer splitting) in addition to one-dimensional sheets originating from the oxygen chains. The Fermi surface shown in Fig. 3d is the structure that one would naively expect in the absence of pseudogap physics and charge density wave ordering, which can alter/fold the electronic structure. In the absence of a band structure calculation for YBCO ortho-VIII, we have taken the LDA prediction for the ortho-II [28] (which has almost the same doping concentration) and un-folded the reconstruction due to the oxygen ordering [66].

It should be noted that both bonding and anti-bonding bands are expected to have a weak but significant k_z dependence in the anti-nodal region [64, 67]. The coupling vectors between the bonding bands in the anti-nodal region are therefore consistent with the three-dimensional ordering vectors $(\delta_1, 0, \pm 0.5)$ and $(\delta_2, 0, \pm 0.5)$ – see Fig. S6. The $\ell = \pm 0.5$ component is also favoured by Coulomb effects (but at the expense of additional elastic energy of lattice distortion).

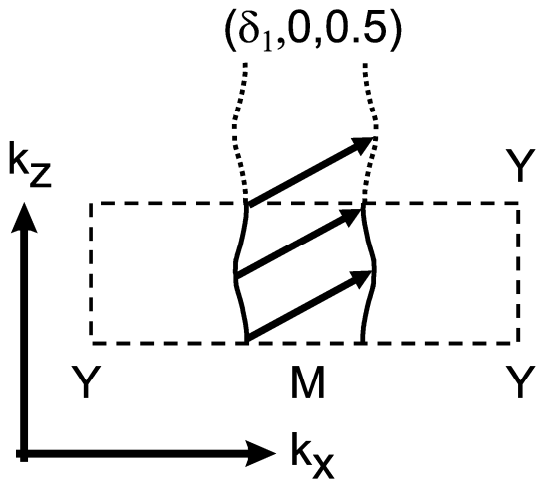

Figure S6: k_z dispersion of Fermi surface related to nesting vector

Schematic representation of the cross-section of the bonding-band Fermi surface as it cuts a face of the Brillouin zone (marked with dashed lines), showing dispersion along the ***c**** direction. This gives better nesting if there is a component 0.5 rlu along ***c****, and will also be favoured by Coulomb effects [40].

Plane-centred versus chain-centred distortions

The "bilayer-centred" structure (Fig. 3a) has maximum amplitude at the CuO_2 bilayer, with displacements in the two layers moving in phase. In contrast the "chain-centred" model (Fig. 3b) has maximum amplitude on the CuO chains and a smaller and antiphase displacement of the two halves of each CuO_2 bilayer. This "chain-centred" model would be favoured by Coulomb interactions between the two halves of a bilayer. However, the symmetry of the wavefunctions of the conduction electrons in the bilayer is an important consideration in deciding between these two models. The bonding (B) conduction band is constructed from states with wavefunctions that are even about the yttrium plane, whereas the antibonding (A) conduction band wavefunctions are odd.

The bilayer-centred model would give a perturbing potential that is even about the Y plane, and hence would most strongly mix B states with B (and A with A). This mixing would create a conduction electron charge density that is even about the Y plane. The bilayer-centred model would connect together the B states at the Fermi level, which are the states we are proposing are involved in the CDW (see Fig. 3d). It is important to note that the bilayer-centred model predominantly connects states that have the same energy – whether they are B or A – and whether they are at the Fermi level or not, so the CDW influence is likely to be strong throughout the Brillouin zone; the importance of this consideration was pointed out by Johannes and Mazin [45].

In contrast, the chain-centred model would give a perturbing potential that is odd about the Y plane, and hence would preferentially mix B states with A (and vice versa). As would be expected, this mixing would give a conduction electron charge density that is odd about the Y plane. However, this model would only weakly connect together the B states at the Fermi level. The chain-centred model predominantly connects states that are of different energy, so the mixing and the CDW influence would likely be weak all through the Brillouin zone. The chain-centred model is unlikely to create gaps at the Fermi level unless the CDW interaction is stronger than the A-B band splitting. In this case, it would probably be too strong to be affected by superconductivity, but this is what we observe. Hence, of the two models fitting the data, we regard the bilayer-centred one as more likely if the coupling of states near the Fermi level drives the CDW transition.

Two additional comments need to be made. Firstly, as pointed out in Refs. 40 and 45, a CDW does not necessarily have to occur at a nesting vector. We await first-principles calculations with interest, to establish whether nesting is important in the present case. Secondly, if the ortho-VIII ordering were perfect, we would expect it to contribute band gaps. However, the short correlation length of this order (see section S3) and the similarity of the values of δ_1 and δ_2 suggest that this influence is minor, and limited to establishing the doping level (and providing disorder which may pin the CDW).

S10: FERMI SURFACE RECONSTRUCTION AND THE LOW TEMPERATURE HEAT CAPACITY

It is difficult to reconcile the LDA-calculated Fermi surface of the underdoped cuprates with quantum oscillation measurements. The observation of an incommensurate charge density wave provides a mechanism for Fermi surface reconstruction [67-71]. The following points should be noted:

1) It is widely accepted from quantum oscillation experiments that there is a drastic change in Fermi surface geometry with doping from large sheets in the overdoped regime to small pocket(s) in the undoped region of the cuprate phase diagram [9, 10, 63, 72]. The pocket area is ~2% of the Brillouin zone, corresponding to an FS calliper ~ $0.14 \times 2\pi / a$.
2) Thermo-electric (Nernst and Seebeck) and Hall angle transport measurements [10, 11, 26, 33, 73] are consistent with a small electron-like pocket in the underdoped region at low temperatures; this supports the assertion in 1).
3) The frequencies F observed in quantum oscillation measurements in $YBa_2Cu_3O_{6+x}$ do not vary dramatically from p≈0.09 with F = 530 T [9] to F=560 T at p≈0.12 [72].
4) The wavevector of the CDW observed in our measurements and those of Refs. [14] and [32] varies little with doping, making it a strong candidate for having a role in forming the small Fermi surface pockets observed.
5) The magnitude of the pseudogap varies rapidly with doping so that it is unlikely that the pseudogap alone is responsible for pocket formation.
6) Our estimates in the previous sections show that, despite its small amplitude, the CDW should affect the electronic structure on an energy scale of 10-20 meV i.e. larger than eB/m^* ≈ 4 meVand sufficient to cause the reconstruction observed by quantum oscillations and indicated by transport measurements below 200 K.

Various calculations [67-71] predict the formation of small Fermi surface pocket(s) which would naturally explain the low frequency orbits observed in quantum oscillation studies. If the pocket(s) were of electron character, this would explain the negative Hall and Seebeck effects [10, 73] observed at low temperature, although it has also been argued that hole pockets could give rise to the negative transport co-efficients observed [74].

Any pocket formation scenario would need to agree with recent heat capacity measurements by Riggs *et al*. [27] on $YBa_2Cu_3O_{6.56}$. These authors have isolated the electronic specific heat $\gamma = \lim_{T\to 0} \frac{C}{T}$ over a wide range of magnetic fields. They claim that γ is unsaturated at high field and ranges from 1.85 mJ K^{-2} mole^{-1} at 0 T to ≈ 5 mJ K^{-2} mole^{-1} at 45 T. It can be shown that γ depends on the electron mass m^* measured by quantum oscillation measurements, where

$$m^* = \frac{\hbar^2}{2\pi} \oint \frac{dk}{|\nabla \varepsilon_k|}, \qquad \text{giving} \qquad \gamma = \alpha \sum_i n_i \frac{m_i^*}{m_e}, \tag{S17}$$

where $\alpha = \frac{\pi a^2 k_B^2 m_e}{3\hbar^2}$ =1.46 mJ K^{-2} mole^{-1}.

The sum is over the Fermi surface sheets, where n_i is the number of closed sheets in the first Brillouin zone (the contribution of open sheets to γ must be calculated separately). There are two

CuO_2 planes per unit cell which give rise to the bonding and antibonding Fermi surface sheets (see section S9). Both of these sheets might produce Fermi surface pockets. We reproduce some of the possibilities below, following the presentation in Ref. [27]. A very interesting scenario (#5) is that presented in Ref. [70] in which the orbit arises from four pieces of Fermi surface connected by the CDW. Scenarios 3 to 5 are closest to what is seen with ARPES and could result from a combination of pseudogap physics and a CDW reconstruction of the FS.

TABLE S1: Estimation of the electronic specific heat.
Electronic specific heat is evaluated using equation (S17) where the quasiparticle mass $m^*/m_e = 1.34$ was obtained from the quantum oscillation in the electronic specific heat in $YBa_2Cu_3O_{6.56}$ [27]. Scenario 1, assuming a single Fermi pocket, gives a lower bound for the electronic specific heat. Scenarios 2-5 are all in reasonable agreement with the experimentally extracted value of γ in high magnetic fields.

Scenario	n_i (A=anti-bonding, B=bonding)	m^* (m_e)	γ(mJ K^{-2} mole^{-1})
1	1 pocket (α or β, on A **or** B sheet)	1.34	1.9
2	2 pockets (α or β, on A **and** B sheets)	1.34	3.8
3	2 pockets (γ on A or B sheets)	1.34	3.8
4	4 pockets (δ on A or B sheets)	1.34	7.6
5	2 pockets (due to a breakdown orbit, not shown, on A and B sheets) [70]	1.34	3.8

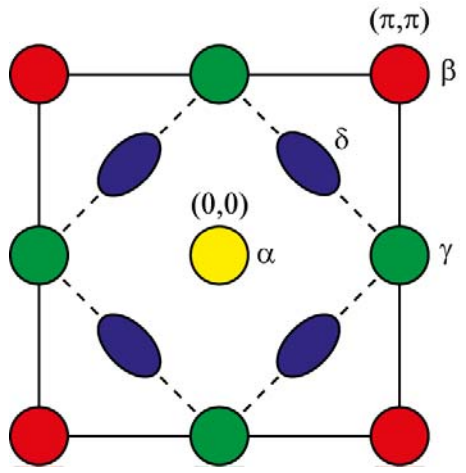

Figure S7: Schematics of some Fermi surface sheets proposed for underdoped YBCO.
Sketches of possible Fermi surface sheets after reconstruction in an underdoped cuprate. Note orbit in scenario 5 is not shown.
(α) Single pocket e.g. [28].
(β) Hole pockets centered at (π,π) [75].
(γ) Electron pockets centred at (π,0) [67].
(δ) Nodal pockets at ($\pi/2$,$\pi/2$) [76].

Although we cannot, at this stage, give a definitive model for the formation of the pockets, the arguments above strongly indicate that the CDW is involved, and ARPES results indicate that simple band structure calculation (even including a CDW), but without including pseudogap physics, is an inadequate tool to account for the small FS pocket.

References for Supplementary Information

[34] Holmes, A. T., *et al.*, A 17 T horizontal field cryomagnet with rapid sample change designed for beamline use. *Rev. Sci. Inst.* **83**, 023904 (2012).

[35] Bouchard, R. *et al.*, A Triple-Crystal Diffractometer for High Energy Synchrotron Radiation at the HASYLAB High Field Wiggler Beamline BW5. *Journal of Synchrotron Radiation* **5**, 90-101 (1998).

[36] Keitel, S. *et al.*, $Si_{1-x}Ge_x$ gradient crystals: a new monochromator material for hard X-rays. *Nuclear Instruments and Methods in Physics Research A* **414**, 427-430 (1998).

[37] Keitel, S. *et al.*, Diffraction of 100 to 200 keV X-rays from an $Si_{1-x}Ge_x$ gradient crystal: comparison with results from dynamical theory. *Acta Cryst.* **A55**, 855-863 (1999).

[38] de Fontaine, D., Ceder, G. and Asta, M., Low-temperature long-range oxygen order in $YBa_2Cu_3O_z$. *Nature* **343**, 544-546 (1990).

[39] de Bergevin, F., and Brunel, M., Observation of magnetic superlattice peaks by X-ray diffraction on an antiferromagnetic NiO crystal. *Phys. Lett. A* **39**, 141-142 (1972).

[40] Grüner, G., Density waves in solids, Addison-Wesley(1994).

[41] Loram, J. W., Mirza, K. A., and Freeman, P. F., The electronic specific heat of $YBa_2(Cu_{1-x}Zn_x)_3O_7$ from 1.6 K to 300 K. *Physica C* **171**, 243-256 (1990).

[42] Castelanni, C., Di Castro, C., and Grilli, Singular Quasiparticle Scattering in the Proximity of Charge Instabilities. M. *Phys. Rev. Lett.* **75**, 4650-4653 (1995).

[43] White, S. R., and Scalapino, D. J., Phase separation and stripe formation in the two-dimensional *t-J* model: A comparison of numerical results. *Phys. Rev. B* **61**, 6320-6326 (2000).

[44] Emery, V. J., Kivelson, S. A., and Lin, H. Q., Phase separation in the *t-J* model.*Phys. Rev. Lett.* **64**, 475-478 (1990).

[45] Johannes, M. D., and Mazin, I. I., Fermi surface nesting and the origin of charge density waves in metals. *Phys. Rev. B* **77**, 165135 (2008).

[46] Roa, J. J., *et al.*, Nanoindentation of Bridgman YBCO samples. *Ceramics International* **38**, 2035-2042 (2012).

[47] Long, M. W. suggested this approach.

[48] Ilakoval, V., *et al.*, High pressure study of $YBa_2Cu_3O_{7-\delta}$ single crystals. *Phys. Lett. A* **161**, 314-318 (1991).

[49] Andersen, O. K., *et al.*, LDA energy bands, low-energy Hamiltonians, *t', t'', t⊥(**k**),* and *J⊥*. *J. Phys. Chem. Solids*, **56**, 1573-1591 (1995).

[50] Kopec, T. K., Competition between charge ordering and superconductivity in $La_{2-x}M_xCuO_4$. *Ann. Phys. Fr.* **13**, 431-435 (1988).

[51] Zhang, Ying, Demler, Eugene and Sachdev, Subir , Competing orders in a magnetic field: Spin and charge order in the cuprate superconductors. *Phys. Rev. B* **66**, 094501 (2002).

[52] Wu, Jian-Bao , Pei, Ming-Xu and Wang, Qiang-Hua, Competing orders and interlayer tunneling in cuprate superconductors: A finite-temperature Landau theory. *Phys. Rev. B* **71**, 172507 (2005).

[53] Fernandes, R. M. and Schmalian, J., Competing order and nature of the pairing state in the iron pnictides. *Phys. Rev. B* **82**, 014521 (2010).

[54] Balseiro, C. A., and Falicov, L. M., Superconductivity and charge-density waves. *Phys. Rev. B* **20**, 4457-4464 (1979).

[55] Machida, K., Charge Density Wave and Superconductivity in Anisotropic Materials. *J. Phys. Soc. Jpn.* **53**, 712-720 (1984).

[56] Gabovich, A. M. and Voitenko, A. I., Model for the coexistence of *d*-wave superconducting and charge-density-wave order parameters in high-temperature cuprate superconductors. *Phys. Rev. B* **80**, 224501 (2009).
[57] Gabovich, A. M., *et al.*, Competition of Superconductivity and Charge Density Waves in Cuprates: Recent Evidence and Interpretation. *Adv. Condens. Matter Physics* 681070 (2010).
[58] Loram, J. W., Mirza, K. A., Cooper, J. R., and Liang, W. Y., Electronic specific heat of $YBa_2Cu_3O_{6+x}$ from 1.8 to 300 K. *Phys. Rev. Lett.* **71**, 1740-1743 (1993).
[59] Chandra, P., Fluctuation effects on the Pauli susceptibility at a Peierls transition. *J. Phys.: Condens. Matter* **1** 10067-10080 (1989).
[60] Lake, B. *et al.*, Three-dimensionality of field-induced magnetism in a high-temperature superconductor. Nature Materials **4**, 658-662 (2005).
[61] Rosso, A., and Giamarchi, T., X-ray diffraction of a disordered charge density wave. *Phys. Rev. B* **68**, 140201(R) (2003)
[62] Vignolle, B., *et al*., Quantum oscillations in an overdoped high-T_c superconductor. *Nature* **455**, 952-955 (2008).
[63] Platé, M., *et al.*, Fermi Surface and Quasiparticle Excitations of Overdoped $Tl_2Ba_2CuO_{6+\delta}$. *Phys. Rev. Lett.* **95**, 077001 (2005).
[64] Markiewicz, R. S., Sahrakorpi, S, Lindroos, M., Lin, H., and Bansil, A, One-band tight-binding model parametrization of the high-*Tc* cuprates including the effect of *kz* dispersion. *Phys. Rev. B* **72**, 054519 (2005).
[65] Fournier, D., *et al*., Loss of nodal quasiparticle integrity in underdoped $YBa_2Cu_3O_{6+x}$. *Nature Physics* **6**, 905–911 (2010).
[66] Sassa, Y., *et al.*, Revealing the ortho-II Band Folding in $YBa_2CuO_{7-\delta}$ Films. *Phys. Rev. B*, **83**, 140511 (2011).
[67] Garcia-Aldea, D., and Chakravarty, S., Multiple quantum oscillation frequencies in $YBa_2Cu_3O_{6+\delta}$ and bilayer splitting. *New J. Phys.* **12,** 105005 (2010).
[68] Mills, A. J. and Norman, N. R., Antiphase Stripe Order as the Origin of Electron Pockets Observed in $1/8$-Hole-Doped Cuprates, Phys. Rev. B 76, 220503(R) (2007)
[69] Yao, H., Lee, D.-H., and Kivelson, S. A., Fermi-surface reconstruction in a smectic phase of a high-temperature superconductor. *Phys. Rev. B* **84**, 012507 (2011).
[70] Harrison, N. and Sebastian, S. E., Fermi surface reconstruction from bilayer charge ordering in the underdoped high temperature superconductor $YBa_2Cu_3O_{6+x}$, arXiv:1206.0053
[71] Sebastian, S. E., Harrison, N. and Lonzarich, Towards resolution of the Fermi surface in underdoped high-T_c superconductors, G. G., Rep. Prog. Phys. **75** *in press* (2012) (*arXiv*:1112.1373)
[72] Singleton, John et al., Magnetic Quantum Oscillations in $YBa_2Cu_3O_{6.61}$ and $YBa_2Cu_3O_{6.69}$ in Fields of Up to 85 T: Patching the Hole in the Roof of the Superconducting Dome, *Phys. Rev. Lett.* **104**, 086403 (2010).
[73] Chang, J., *et al.*, Nernst and Seebeck coefficients of the cuprate superconductor $YBa_2Cu_3O_{6.67}$: a study of Fermi surface reconstruction. *Phys. Rev. Lett.* **104**, 057005 (2010).
[74] Tranquada, J. M., Basov, D. N., LaForge, A. D., and Schafgans, A. A., Interpreting quantum oscillation experiments on underdoped $YBa_2Cu_3O_{6+x}$. *Phys. Rev. B* **81**, 060506 (2010).
[75] Vignolle, B., *et al.*, Quantum oscillations in an overdoped high-Tc superconductor. *Nature* **455**, 952-955 (2008).
[76] Lee, P. A., From high temperature superconductivity to quantum spin liquid: progress in strong correlation physics. *Rep. Prog. Phys.* **71**, 12501 (2008).